Recoil-ion charge-state distribution following the β^+ decay of ^{21}Na

N. D. Scielzo and S. J. Freedman
Department of Physics, University of California at Berkeley and Lawrence Berkeley National Laboratory, Berkeley, California 94720, USA

B. K. Fujikawa and P. A. Vetter
Lawrence Berkeley National Laboratory, Berkeley, California 94720, USA

(Received 3 January 2003; revised manuscript received 21 April 2003; published 29 August 2003)

The charge-state distribution following the β^+ decay of ^{21}Na has been measured, showing a larger than expected fraction of the daughter ^{21}Ne in positive charge states. No dependence on either the β^+ or recoil nucleus energy is observed. The data are compared to a simple model based on the sudden approximation. Calculations suggest that a small but important contribution from recoil ionization has significant consequences for precision β decay correlation experiments detecting recoil ions.

DOI: 10.1103/PhysRevA.68.022716 PACS number(s): 32.80.Hd, 23.20.Nx, 13.30.Ce

I. INTRODUCTION

Measurements of recoil-ion spectra in nuclear β decay are useful probes of the weak interaction. The energy spectra of ^{6}He [1–3], ^{23}Ne [1,4], ^{19}Ne [1,5], and ^{35}Ar [1] decays helped lead to the discovery of the $V-A$ (vector minus axial vector) structure. The ^{6}He β-ν correlation [3] provides the best limit on a possible tensor component. Recoil spectra from the electron capture (EC) decay of ^{37}Ar [6] and β^+ decay of ^{38m}K [7] have recently put limits on the admixture of heavy neutrinos.

Trapped radioactive atoms and ions are appealing sources of activity for a new generation of precise β decay experiments testing the standard model. Radioactive nuclei can be confined to a small volume (~ 1 mm^3), decay essentially at rest (velocities $\lesssim 1$ m/s), and the recoil daughters emerge with minimal perturbation. The daughter ions can be manipulated with electric and magnetic fields. Several β decay correlation measurements are currently under way [8,9] or nearing an interesting precision of 0.01 [10], and further improvements are expected.

In interpreting recoil-ion measurements, the charge-state production is assumed to be independent of the β and nuclear recoil energy. For β^+ emitters, ionization mechanisms are essential since positive daughter ions form only when $\geqslant 2$ orbital electrons are lost. Negative ions, if formed, are often unstable and of limited utility for measurements. Ionization affects the statistical precision and leads to systematic errors if dependent on β or recoil-ion energy. For example, ionization dependent on nuclear momentum would alter each charge state's energy spectrum, leading to an experimental signature similar to that of a β-ν correlation.

Understanding the ionization state following β decay is interesting in its own right. For β^- emitters, such as ^{6}He [11], ^{23}Ne [12], ^{85}Kr [13], and ^{41}Ar [14], electron shake-off (SO) resulting from parent/daughter orbital mismatch is the dominant process. The charge-state distribution decreases with increasing charge, with 80–90 % of daughter ions having a charge $+1$ and $<5\%$ with charge $\geqslant 3$. In addition, inner shell vacancies lead to dramatic ionization from Auger cascades in the electron capture decay of ^{37}Ar [15,16], the internal conversion (IC) of ^{131m}Xe [17], and the β^- and IC decay of ^{133}Xe [18].

Until recent experiments with radioactive trapped atoms, there were no data on charge-state production following β^+ emission. The decay of the β^+ emitter ^{79}Kr is predominantly by EC and produces positive ions, neutrals, and negative ions [19]. A simple estimate equating the net electron loss in β^- and β^+ decay indicates that $<5\%$ of the daughters in β^+ decay should be in positive charge states, with the yield decreasing with increasing ion charge state.

Laser trapped ^{38m}K [10] and the present ^{21}Na results show that this greatly underestimates the production of positive ions for these β^+ emitters. We measure the charge-state distribution by detecting the β^+ and recoil ion in coincidence. The majority (94.98 ± 0.13 % [20]) of ^{21}Na β decays (end point energy $E_0 = 2525.7$ keV) proceed directly to the ground state of ^{21}Ne, leading to recoil energies $\leqslant 229$ eV. The remaining 5.02% β decay to the first excited state of ^{21}Ne, which subsequently deexcites through $M1$ emission of a 350.7 keV γ ray. The recoil-energy spectra for these decays (shown in Fig. 1) are calculated using a Monte Carlo simulation described in the text. Electron capture events, which account for $<0.1\%$ of decays, are not detected.

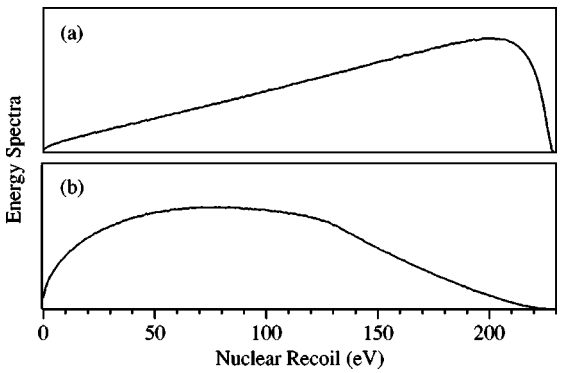

FIG. 1. Calculated recoil-energy spectra (linear scale) following ^{21}Na β decay to (a) the ground state and (b) the first excited state of ^{21}Ne.

We use the relative ^{21}Ne ion abundances to study the dependence of the ionization process on the decay product energies. In the ''sudden approximation,'' electrons are ejected because of orbital mismatch following the sudden change in nuclear charge, and ionization is independent of β energy. However, the energy imparted to shake-off electrons (of the order of the binding energy) reduces the available phase space [21], suppressing low-energy β emission. Ionization in the K shell has significant β energy dependence, especially in the β^- decays of ^{99}Tc [21] and ^{147}Pm [21,22], where the binding energy B_K and E_0 are comparable. In addition, the direct collision (DC) mechanism, in which the β knocks out an orbital electron, is expected to be important for decays with comparable B_K and E_0. Calculations indicate that the DC mechanism can contribute significantly to electron loss at low β energies, even for decays with $B_K/E_0 \ll 1$, and measurements disagree with the calculation unless this DC contribution is included. Therefore, even though shake-off from deeply bound K shells is small, the energy dependence can be significant.

Nuclear recoil has an observable ionizing effect for high-energy γ ray [23], nucleon [23], and α emission [24]. In β decay, recoil ionization is expected to be small in most atoms investigated except ^{6}He, where the large E_0 and small nuclear mass lead to recoil energies up to 1400 eV. Nuclear recoil contributes 3% to the production of $^6Li^{2+}$, and $>50\%$ to the production of $^6Li^{3+}$ [11]. No evidence of recoil ionization was found by comparing the abundances of charge states $+2$ through $+5$ of ^{23}Ne β^- decay at 250 and 450 eV, although the limit is not particularly restrictive [12].

II. TRAPPING APPARATUS

The production and accumulation of ^{21}Na in a magneto-optical trap (MOT) has been described elsewhere [25,26] and will be only briefly summarized here. The ^{21}Na is produced through ^{24}Mg$(p,\alpha)^{21}$Na by bombarding a powdered MgO target with 2 μA of 25 MeV protons from the 88-inch cyclotron at Lawrence Berkeley National Laboratory. The alumina crucible containing the target is heated to 1000 °C, and the sodium diffuses out of the target at a rate of $\approx 3 \times 10^8$ atoms/s. The atomic beam emerges through four narrow, alumina tubes aimed at the trapping chamber. Additional collimation 10 cm downstream from the tubes is provided by two-dimensional optical molasses generated by 1 cm laser beams reflected four times across the atomic beam.

The laser light at 589 nm for the transverse cooling stage and the MOT is generated by two Coherent 899 ring dye lasers using Rhodamine 6G dye. The lasers are frequency stabilized with saturated absorption spectroscopy on the D_2 transition in ^{23}Na after passing through an acousto-optic modulator to account for the 1648 MHz isotope shift. An electro-optic modulator shifts $\approx 10\%$ of the laser power to the $3\,^2S_{1/2}(F=1)$ to $3\,^2P_{3/2}(F=2)$ transition frequency, avoiding optical pumping to the untrapped $3\,^2S_{1/2}(F=1)$ hyperfine level.

A 8 mW/cm^2 slowdown laser beam detuned -20 MHz from the $3\,^2S_{1/2}(F=2)$ to $3\,^2P_{3/2}(F=3)$ transition decelerates the atomic beam as it traverses a 1.2 m long ''Zeeman-slower'' solenoid. A 4 mm diameter ''dark spot'' in the center of the slowdown laser beam creates a shadow over the trap. Keeping the unbalanced force of the slowdown laser beam from destabilizing the trap doubles the number of atoms trapped.

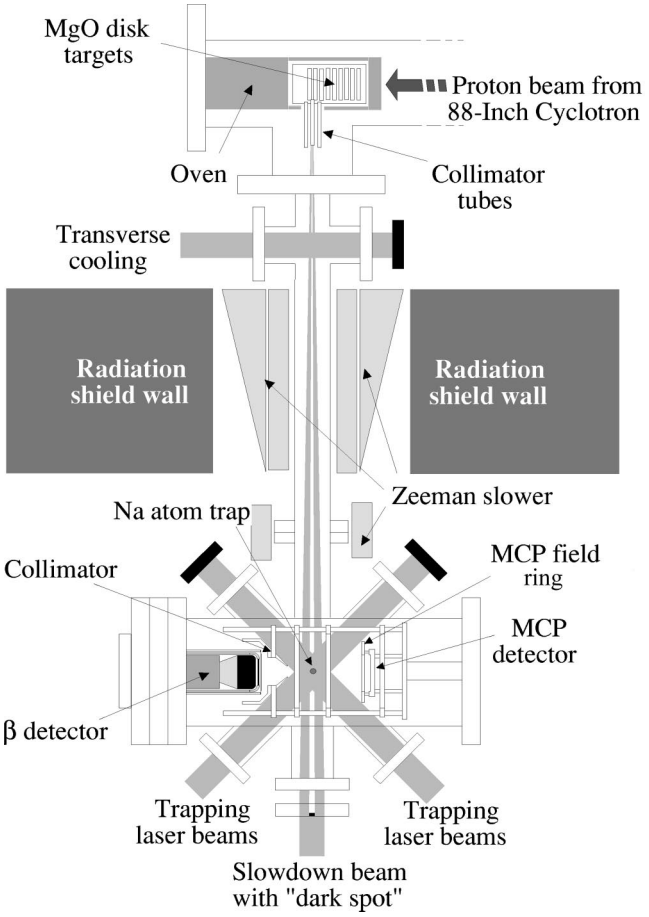

FIG. 2. Experimental arrangement shown is not drawn to scale. Anti-Helmholtz trapping coils (not shown) lie above and below the trapping chamber in the plane of the page. The ΔE and E scintillators are shown in black.

The slow ^{21}Na atoms are captured in a six-beam MOT. The trapping laser beams are 3.5 cm in diameter, have a detuning of -15 MHz, and each has an intensity of ≈ 6 mW/cm^2. Anti-Helmholtz coils surrounding the trap generate a quadrupole field with an axial gradient of 12 G/cm. Up to 8×10^5 ^{21}Na atoms have been trapped. The trap lifetime is 12 ± 2 s. The trap is monitored by measuring fluorescence with a photomultiplier tube (PMT), and the trap position and spatial distribution are recorded with a charge-coupled device camera.

III. MEASUREMENT TECHNIQUE

The experimental arrangement is shown in Fig. 2. The trapped atoms are suspended between two detectors—a ΔE-E plastic scintillator telescope on one side, and a CsI-coated chevron microchannel plate (MCP) detector on the other. A system of stainless steel electrodes generates a static electric field of ≈ 1 kV/cm to guide positive ions from the

trap to the MCP. A trigger in either portion of the β detector telescope opens a 3 μs coincidence window, providing time for the recoil ^{21}Ne to reach the MCP. For coincident events, we record the time between the β detector (either ΔE or E) and MCP trigger, the pulse heights and singles rates from the detectors, and the PMT fluorescence signal.

A. Electric field

Dielectric material within the chamber was minimized so the electric field (and therefore the ion trajectories) could be calculated reliably. Four stainless steel rods hold the collimator and rings in place and supply the voltages to these electrodes, eliminating the need for separate leads. An aluminum ring 10 mm in front of the MCP ensures that the screw heads and detector leads do not influence the electric field, giving a simple surface to model. The electric field was calculated for a three-dimensional 0.5 mm lattice by commercial ion optics software.

The electrode voltages were selected such that $>99.5\%$ of $^{21}Ne^{+}$ (in coincidence with detected β^{+}'s) and all of the higher-charge-state ^{21}Ne ions are drawn into the active area of the MCP detector. In coincidence with β^{+}'s, only $18.5 \pm 0.2\%$ of $^{21}Ne^{0}$ daughters from the trap reach the MCP active area. Temporal separation of the ion peaks allowed independent fits for each charge state. The electric field suppresses backgrounds by establishing a ≈ 1 kV potential barrier for recoil ions originating on the chamber walls. The $^{21}Ne^{0}$ drift time to the MCP from most surfaces is greater than 3 μs. The collimator potential prevents ^{21}Ne ions originating on the Be window from reaching the MCP.

Using the trap-to-MCP distance of 83.08 ± 0.04 mm determined by the $^{21}Ne^{0}$ time of flight, we compared the measured and calculated rising edge of each recoil-ion peak. The agreement is well within the uncertainty of 0.6 ns, implying that the average electric field magnitude along the ion trajectories is accurate to 0.2%.

B. Microchannel plate detector

For ions with kinetic energies ≥ 2 keV, the detection efficiency $\mathcal{E}_{MCP}$ of a MCP operated without a biasing grid shows little variation, regardless of ion species [27] or charge state [28], and approaches the open area ratio of $\approx 60\%$ [27,29–34]. The accelerating potential of 9.0 kV minimizes the energy dependence in $\mathcal{E}_{MCP}$. Calculations indicate that all ions impact the MCP with angles less than 2°. Although $\mathcal{E}_{MCP}$ depends on the angle between the microchannel axis and the particle's momentum, particles that impact the detector at angles less than 5° are detected with essentially uniform probability [29].

After data collection, we conducted an off-line calibration of the MCP detector. Using an ion source, a monoenergetic beam of $^{20}Ne^{+}$ at rates of 10^{3}–10^{4} Hz/cm^2 was generated by sending a defocused beam through several small apertures. A 30 μm thick aluminum collimator with a ≈ 5 mm^2 hole 10 mm in front of the MCP localized the impact area.

We found that the function

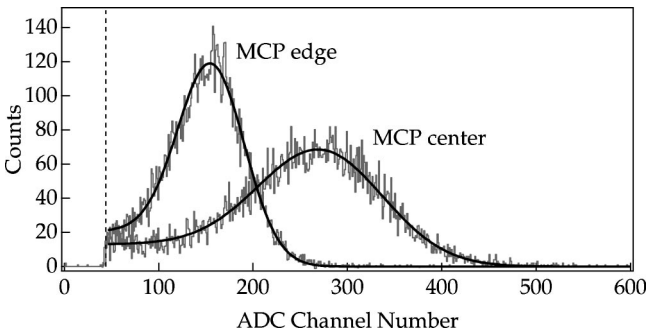

FIG. 3. Representative MCP pulse height distributions for 10 keV $^{20}Ne^{+}$ ions impacting the center and edge of the active area. The smooth curves are the empirical fit to $P(x)$ and the dashed vertical line shows the electronic threshold.

$$P(x) = \frac{N}{1+A}\left[\frac{1}{\sqrt{2\pi}\sigma_0} e^{-(x-x_0)^2/2\sigma_0^2} + \frac{A}{2}\mathrm{erf}\left(\frac{x-x_0}{\sqrt{2}\sigma_0}\right)\right], \tag{1}$$

consisting of a Gaussian distribution with a step function below the peak, adequately describes the $^{20}Ne^{+}$ pulse height distribution (PHD). We estimated $\mathcal{E}_{MCP}$ by multiplying the open area ratio by the fraction of the PHD larger than the electronic threshold. The peak x_0, width σ_0, and step function magnitude A were related empirically by $\sigma_0 \propto x_0$ and $A \propto x_0^{-1}$. Since the normalization N has no impact on detection efficiency, $\mathcal{E}_{MCP}$ could be determined from x_0 alone. Sample spectra are shown in Fig. 3 for 2000 Hz of 10 keV $^{20}Ne^{+}$ ions impacting the center and edge of the MCP detector.

By scanning the MCP across the collimator aperture, the two-dimensional map of the detector response shown in Fig. 4 was generated. The average pulse height decreases as the ions strike the MCP further from the center. At 10 keV, 94–97 % of the PHD was above the 25 mV electronic threshold. A poor signal-to-noise ratio prevented measuring the PHD for $^{20}Ne^{2+}$, so $^{20}Ne^{+}$ accelerated by twice the potential was used. We found that $\mathcal{E}_{MCP}$ changed by less than 2% over the

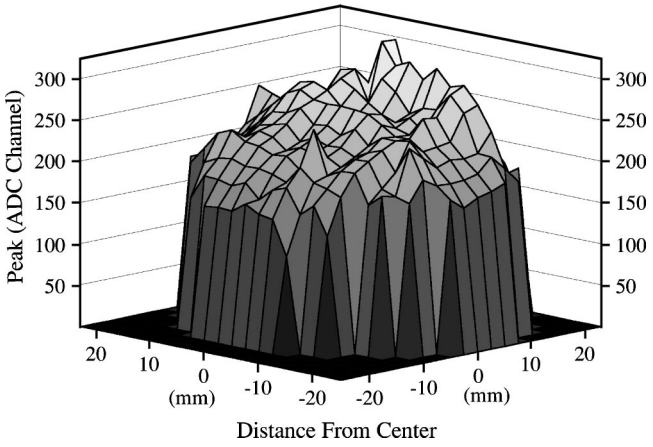

FIG. 4. Two-dimensional distribution of analog-to-digital converter (ADC) peak pulse heights for a 10 keV $^{20}Ne^{+}$ ion beam impacting the MCP. The variation leads to a detection efficiency of 97% near the middle and 94% at the edges. A sharp drop to zero occurs as the beam moves from the active area.

energy range 10–30 keV. Minimal change in the PHD was observed for off-line beams of less than 10^4 Hz/cm^2.

C. β-detector telescope

The β-detector telescope is centered inside a 12.4 cm diameter stainless steel sleeve by an acrylic holder with a 1 mm thick tungsten-alloy ring. This ring stops β^+'s from reaching any part of the β detector other than the scintillator. The only material in the path from the trap to the ΔE scintillator is a 127 μm thick beryllium window (to maintain the ultrahigh vacuum) and one layer of 7.6 μm thick aluminized Mylar. A tungsten-alloy collimator restricts the field of view of the β detector to a narrow cone centered about the trapped atoms, minimizing the number of coincidences from scattered β^+'s. At 1 mm thick, the lip of the collimator stops 3 MeV β^+'s.

The ΔE and E plastic scintillators are 1 mm and 15 mm thick with diameters of 35.5 mm and 45 mm, respectively. The edge of the ΔE scintillator is beveled at 11° to match the maximal angle of incoming β^+'s from the trap. The E scintillator stops all β^+'s from the decay, and its larger diameter minimizes the effects of angular straggling through the ΔE scintillator. Light from the scintillators is piped through separate, acrylic light guides to magnetic field insensitive Hamamatsu R5924 (ΔE) and R5946 (E) PMTs. The scintillators are optically isolated by a single layer of aluminized Mylar, minimizing the dead layer. At 91.9 ± 1.0 mm from the trap, the β detector subtends a solid angle of $0.92 \pm 0.02\,\%$ of 4π.

The β energy is determined from the sum of energies deposited in both detectors. The resolution of the ΔE and E detectors was calibrated using the conversion electron (CE) lines of ^{113}Sn and ^{207}Bi. The ΔE detector limits the resolution, leading to a full width at half maximum (FWHM) of 120 ± 12 keV at the 364 keV CE line of ^{113}Sn and 150 ± 15 keV at the 976 keV CE line of ^{207}Bi.

The β-detector resolution function is not just the simple Gaussian expected from photon statistics. Compton scattering of annihilation radiation produces Compton continua that extend $\approx$340 keV above the β energy. Backscattering and bremsstrahlung result in low-energy tails. These features were calculated using the electron and photon transport code EGSNRC [35] for β^+'s incident upon the center and edge of the detector. The results were convoluted with the measured FWHM resolution and extrapolated between the center and edge because of the difference in average scintillator path lengths traversed by annihilation γ rays. The radial dependence of the light fraction reaching the ΔE PMT was discovered and included in the analysis. The measured efficiency for 511 keV γ rays incident on the E detector from a ^{68}Ga source was $13.0 \pm 1.4\,\%$, in agreement with 13.4% determined using EGSNRC.

A low-energy threshold minimizes the uncertainties associated with the complicated β-detector calibration. The acquisition is triggered by events that deposit $\gtrsim$10 keV in either the ΔE or E detector, although only events that deposit $\geqslant$50 keV in the detector and trigger the ΔE are included in the analysis. After accounting for energy loss in the Be window, we detect β^+'s with energies $\gtrsim$175 keV and only $2.7 \pm 0.1\,\%$ of the spectrum is missed.

D. Monte Carlo simulation

The data are compared to a detailed Monte Carlo simulation that generates the time-of-flight (TOF) spectra from trapped atoms. The nuclear recoil is calculated from the β and ν momenta by conservation of momentum. The lepton momenta are generated from an allowed distribution with the Fermi function included as a cubic spline from the tabulated values in Ref. [36]. Recoil order effects are included using the results of Ref. [37]. To determine the charge-state distribution, we assume the conserved vector current hypothesis and the absence of second-class currents. Order-α radiative effects are included according to the prescription outlined in Ref. [38], which properly accounts for the four-body final state from emission of a hard bremsstrahlung photon.

We use 5.02% for the branching ratio to the ^{21}Ne $(5/2^+)$ excited state [20] and the standard model values for both β-νcorrelations. For decays to the excited state, we include order-α radiative effects but not recoil order terms because of uncertainty in their sign. The omission of recoil order corrections, the excited-state lifetime, and the β-γ correlation is inconsequential.

For β^+'s that intersect the scintillator volume, the ion trajectory is calculated in the electric field using a commercial ion optics program. The ion's TOF, energy, and position are recorded upon MCP impact. Energy loss and scattering in the Be window, although small, become significant at low energies and are calculated using EGSNRC and included in the Monte Carlo simulation. The measured energy and position dependent acceptance functions for the MCP and β detectors are applied.

The acquisition detects only the first MCP trigger following any β-detector trigger. This introduces a slight bias for events with short TOFs. Lost true and accidental coincidences are corrected for in the analysis using average β-detector and MCP trigger rates of 4 kHz [39].

Small ($\leqslant 1\%$) contributions from β^+'s that scatter off the collimator tip or the MCP are modeled and included in the analysis. The TOF distribution for γ-^{21}Ne coincidences is determined from events that trigger the E but not the ΔE detector. The magnitude of this spectrum is scaled by the relative detection efficiency of the ΔE and E for 511 keV γ rays.

Internal conversion of the excited-state γ ray causes the excited-state contribution in each charge state to deviate from the β decay branching ratio. We calculate this effect using IC coefficients computed as a function of γ ray energy using relativistic atomic wave functions and a finite nuclear radius [40]. Electron loss following inner shell vacancies is incorporated using the results of Ref. [41]. The correction increases rapidly with charge state, changing the excited-state branching ratio by -0.0075%, -0.006%, $+0.14\%$, $+0.81\%$, and $+5.7\%$ for charge states 0, +1, +2, +3, and +4, respectively.

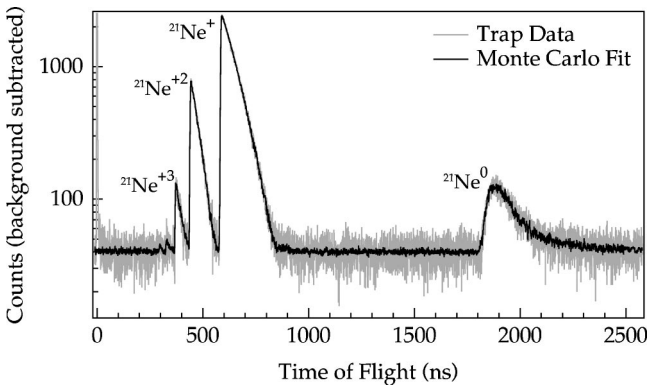

FIG. 5. Recoil ^{21}Ne time-of-flight spectrum. The inclusion of the experimental γ-^{21}Ne coincident TOF spectrum in the fit leads to the noise in the background level.

IV. EXPERIMENTAL RESULTS

The measured time-of-flight recoil spectrum in Fig. 5 clearly reveals the ^{21}Ne charge states. The detector is far more sensitive to positive ions than to neutral atoms, and it can detect negative ions with electric fields reversed. As discussed below, we found no evidence of negative ions, and $^{21}Ne^{0}$, despite being the most prevalent, has the smallest absolute detection efficiency and largest uncertainties. With knowledge of the source activity and the detection efficiency for positive ion and β^{+} coincidences, the entire charge-state distribution is reconstructed.

A. Negative neon state

If all orbital electrons were retained, $^{21}Ne^{-}$ would be formed. A calculation based on a nonrelativistic fixed-core valence-shell configuration interaction predicts the existence of a metastable Ar^{-} state, but the metastable Ne^{-} state is expected to decay to the continuum through an $E1$ transition [42]. Direct searches found Ar^{-} with a lifetime of $\sim$350 ns, and conclude that if Ne^{-} exists its lifetime is much less than 50 ns [43], in agreement with the calculation. Even if Ne^{-} were metastable with an appreciable lifetime, the probability of remaining negatively charged is small. The calculated metastable Ne^{-} configuration ($1s^2 2s^2 2p^5 3p^2$) is not accessible from the ground states of Na because of symmetry. However, due to the $3s \leftrightarrow 3p$ cycling from the trapping lasers, $\approx$30% of the population has the configuration $1s^2 2s^2 2p^6 3p^1$. Since the overlap between the Na $2p$ and Ne $2p$ states is 97%, each $2p$ electron has less than a 3% chance of being shaken up to the $3p$ state. Therefore, the branching ratio for this configuration should be less than 5.4%. Moreover, with a lifetime much less than 50 ns, $^{21}Ne^{-}$ would be difficult to distinguish from $^{21}Ne^{0}$. We conducted a direct search by reversing the direction of the electric field and found no evidence of β^{+}-$^{21}Ne^{-}$ coincidences or of β^{+}-$^{21}Ne^{0}$ coincidences at shorter than kinematically allowed TOFs. The limits as a function of branching ratio are shown in Fig. 6. We conclude that $^{21}Ne^{-}$ is not a significant charge state.

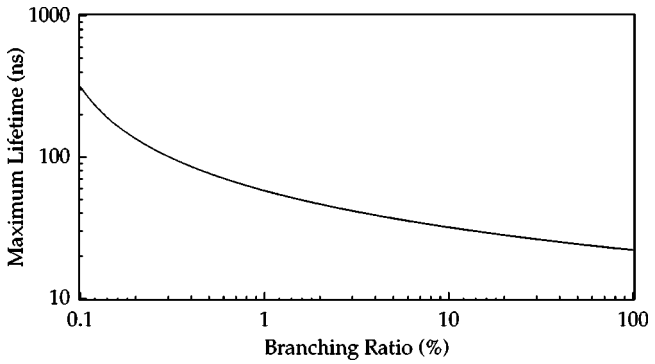

FIG. 6. Maximum lifetime of $^{21}Ne^{-}$ vs its β decay branching ratio (68% C.L.), assuming that the MCP detection efficiency decreases linearly at energies below 2 keV.

B. Neutral neon

The majority of ^{21}Ne daughters are neutral with recoil energies of $\leqslant$229 eV. At energies below 1 keV, $\mathcal{E}_{MCP}$ is energy dependent and much smaller than at keV energies. Studies of $^{16}O^{0}$, $^{16}O^{+}$, and $^{16}O^{-}$ with energies between 30 and 1000 eV indicate that detection efficiencies depend on charge state but fall nearly linearly with decreasing energy [44]. However, $^{21}Ne^{0}$ strike the MCP with angles as large as 15° so their detection efficiency is expected to vary greatly with impact angle. The neutral branching ratio of 78.0 $\pm$3.1 % is determined by subtracting the ion branching ratios (discussed below) from unity. We find the average intrinsic MCP detection efficiency to be 6.1 ± 0.8 %, which is consistent with results in Ref. [44] for $^{16}O^{0}$.

C. Absolute charge-state distribution

The relative branching ratios for the positive charge states are determined by fits to a Monte Carlo simulation. The results are shown in Table I. The absolute branching ratios are determined from the source strength and detection efficiency for β^{+}-^{21}Ne coincidences. The branching ratio Γ_q is given by

$$\Gamma_q = \frac{R_q}{R_T}, \tag{2}$$

where R_q is the detection rate of ion recoils with charge $+q$, and R_T is given by

TABLE I. Ratio of production of positive ions relative to $^{21}Ne^{+}$ production. Corrections for MCP detection efficiency as well as dead-time losses have been taken into account. The production ratio for ions with charge $\geqslant 6$ is $\leqslant 0.0003$.

Ions compared	Production ratio
$^{21}Ne^{2+}$: $^{21}Ne^{+}$	0.1673 ± 0.0011
$^{21}Ne^{3+}$: $^{21}Ne^{+}$	0.0143 ± 0.0003
$^{21}Ne^{4+}$: $^{21}Ne^{+}$	0.0013 ± 0.0003
$^{21}Ne^{5+}$: $^{21}Ne^{+}$	0.0006 ± 0.0003

TABLE II. Relevant values and uncertainties in the quantities needed for calculating the charge-state branching ratios.

Quantity	Value	Uncertainty
N	269 000	29 000
$\tau_{1/2}$ (s)	22.48	0.04
Ω_{MCP}	0.996	0.001
Ω_{β}	0.0092	0.0002
$\mathcal{E}_{MCP}$	0.58	0.05
$\mathcal{E}_{\beta}$	0.973	0.001
L	0.95	0.01
R_{1+} (Hz)	7.58	0.01
R_T (Hz)	40.9	5.7
Γ_{1+}	0.186	0.026

$$R_T = \frac{N \ln 2}{\tau_{1/2}} \Omega_{MCP} \Omega_{\beta} \mathcal{E}_{MCP} \mathcal{E}_{\beta} L. \tag{3}$$

Here N is the average number of ^{21}Na atoms in the trap, $\tau_{1/2}$ the half life, Ω_{MCP} and Ω_{β} the detector solid angles, $\mathcal{E}_{MCP}$ and $\mathcal{E}_{\beta}$ the detection efficiencies, and L the fraction of detector lifetime. These values and associated uncertainties are shown in Table II. The neutral branching ratio is determined by subtraction. N is estimated from the trap fluorescence F by

$$N = \frac{F}{R \Omega_{ph} C}, \tag{4}$$

where Ω_{ph} is the PMT solid angle, and C is the efficiency. The intensity of radiated light is

$$R = \frac{\Gamma}{2} \frac{s}{1 + s + 4(2\pi\delta)^2/\Gamma^2} \tag{5}$$

with saturation parameter s natural linewidth Γ, and detuning of laser light δ.

D. Comparison with ^{23}Ne β^- decay

Figure 7 shows a comparison of the daughter charge-state distribution following ^{21}Na β^+ decay with that for β^- decay of ^{23}Ne. One might expect the β^+ charge-state distribution to be similar to the β^- distribution shifted by a charge of $+2$ because of the difference in ΔZ. The branching ratios, however, are similar when shifted by one unit of charge. This implies that an extra electron, most likely the valence electron, is frequently lost in ^{21}Na β^+ decay, leading to multiple electron loss following $22.0 \pm 3.1\%$ of decays instead of $\approx 5\%$.

E. Dependence of charge-state distribution on energy of decay products

In neon, 99% of K-shell vacancies lead to subsequent Auger transitions [41], so they contribute significantly to the production of $^{21}Ne^{2+}$ ($\approx 30\%$) but not $^{21}Ne^{+}$ ($<0.1\%$), in the model discussed below. We do not expect $^{21}Ne^{+}$ production to exhibit observable β energy dependence, although higher charge states may. The ratio of $^{21}Ne^{2+}$ to $^{21}Ne^{+}$ production as a function of β energy is therefore sensitive to the energy dependence of the ionization of the K shell. The large ratio of the Q value to B_K in ^{21}Na (>2500) ensures that the β decay phase space is minimally impacted. A calculation using nonrelativistic hydrogenic wave functions for the ^{21}Ne K shell [45] demonstrates that, even if all ionization resulted from K-shell electron loss, the systematic effect for β decay correlations in ^{21}Na would be less than 0.1%.

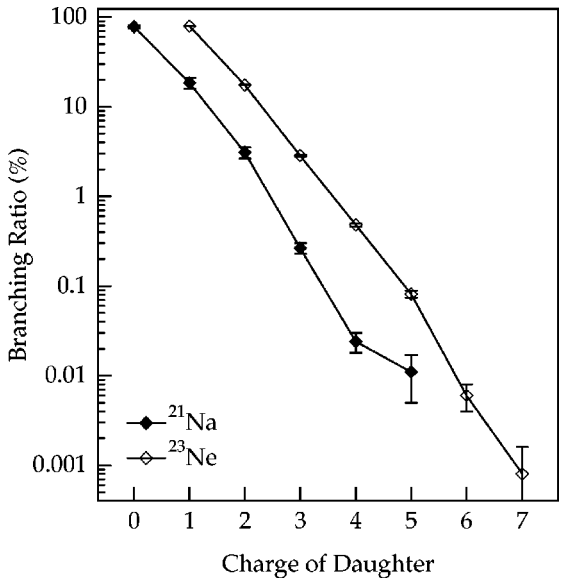

FIG. 7. Comparison of charge-state distributions of ^{21}Na and ^{23}Ne. Points are connected to guide the eye.

The ratio of K-shell electrons ejected per decay by direct collisions $[P_K(\mathrm{DC})]$ versus shake-off $[P_K(\mathrm{SO})]$ for a decay with a mean β kinetic energy of $\overline{E_{\beta}}$ was first estimated by Feinberg [46] to be

$$\frac{P_K(\mathrm{DC})}{P_K(\mathrm{SO})} \approx \frac{B_K}{\overline{E_{\beta}}}. \tag{6}$$

However, more recent calculations have shown that the DC mechanism in β^+ decays with end-point energies of ~ 1 MeV is enhanced by 15–20 times beyond this estimate [47,48]. A comparable enhancement in ^{21}Na would give a contribution to K-shell ionization of $\sim 1\%$.

In β^+ emitters [49–52], P_K has been measured only over an average of the β energy distribution by detecting K-shell x rays in coincidence with annihilation γ rays to isolate β^+ from EC decays. We measured the energy dependence in the ion charge-state yields. Any increase in charge-state ratios at low energies in Fig. 8 could be a signature of direct collisions. Assuming the β energy dependence predicted by Feinberg [53], the DC mechanism contributes less than 1.3% to the production of $^{21}Ne^{2+}$ ions and less than 4.3% to the production of $^{21}Ne^{3+}$ ions.

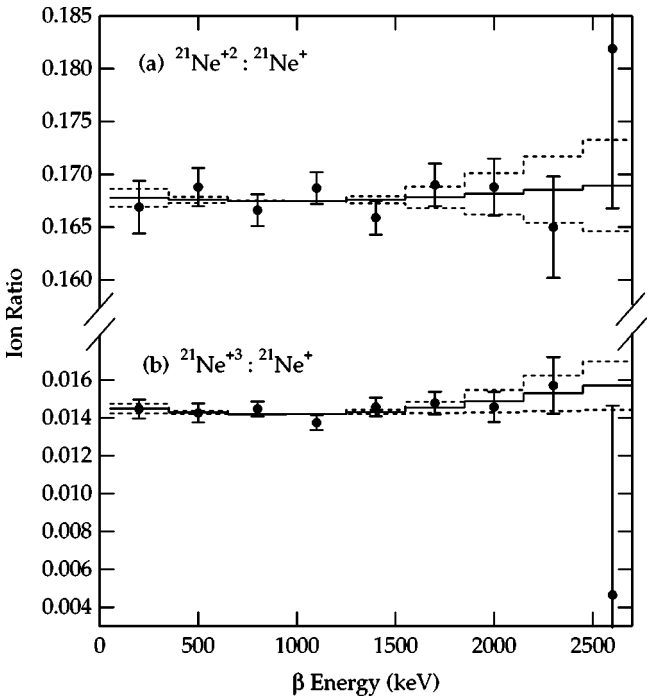

FIG. 8. Ratio (a) $^{21}Ne^{2+}:{}^{21}Ne^{+}$ and (b) $^{21}Ne^{3+}:{}^{21}Ne^{+}$ versus total energy deposited in β detector. Note the scale change between (a) and (b). The energy extends beyond the ^{21}Na end point because of interactions between annihilation γ rays and the scintillator volume. A correction has been applied because the collection efficiency for $^{21}Ne^{+}$ in coincidence with low-energy β^{+}'s is slightly less than 100%. A horizontal line would indicate the absence of β and recoil energy influence on ionization. The solid line shows the best fit for recoil ioinization, while the dashed line shows $\pm 1\sigma$ fits (for a fixed ratio at 1100 keV). The fits yield a $1.3\pm 3.9\,\%$ and a $16\pm 14\,\%$ recoil ionization contribution for $^{21}Ne^{2+}:{}^{21}Ne^{+}$ and $^{21}Ne^{3+}:{}^{21}Ne^{+}$, respectively.

The β^{+} energy also gives information about the daughter nucleus recoil energy. At intermediate energies the momenta of the β and ν can cancel, causing minimal nuclear recoil. The ion ratios $^{21}Ne^{2+}:{}^{21}Ne^{+}$ and $^{21}Ne^{3+}:{}^{21}Ne^{+}$ in Fig. 8 are essentially consistent with no recoil ionization, with contributions of $1.3\pm 3.9\,\%$and $16\pm 14\,\%$, respectively. These limits for β^{+} decay are not stringent enough for current precision β decay work or to test the predictions of the calculation described below. For this, recoil ionization needs to be studied at the level of $\lesssim 1\%$.

There is no indication that the number of trapped atoms, which ranged from 100 000 to 500 000, influenced the results. Scattering cross sections for recoil ions or β^{+}'s emerging from the cloud of trapped atoms should be much less than 10^{-13} cm^2, several orders of magnitude too small to influence the charge-state distributions. Charge exchange would create $^{21}Na^{+}$ essentially at rest, giving a narrow TOF peak at 728 ns that is not seen. At the highest ion collection rates, the average MCP output decreased by $9\pm 2\,\%$, and we attribute this to local electric field distortions from charge extraction in active channels [54]. This decreased $\mathcal{E}_{MCP}$ by 0.36% for ions and $10\pm 3\,\%$ for neutrals, because of their small MCP signals. After correcting for this effect, all charge-state production ratios remain constant regardless of trap population. Assuming a linear dependence on trap population, we find differences in $^{21}Ne^{0}:{}^{21}Ne^{+}$, $^{21}Ne^{2+}:{}^{21}Ne^{+}$, and $^{21}Ne^{3+}:{}^{21}Ne^{+}$ between the smallest and largest traps of $(0.6\pm 3.0)\%$, $(0.4\pm 1.5)\%$, and $(2.3\pm 7.5)\%$, respectively.

V. CALCULATIONS

Electron shake-off is calculated using the "sudden approximation" as the nuclear charge changes and the nucleus receives a momentum kick from the decay. The probability of finding an electron (originally in orbital ψ_i of a nucleus of charge Z) in orbital ψ_f' of charge $Z+\Delta Z$ is

$$P_{if}(\vec{k}_r)=|\langle\psi_i|e^{-i\vec{k}_r\cdot\vec{x}}|\psi_f'\rangle|^2. \tag{7}$$

In the rest frame of the nucleus of mass M, the electrons (of mass m_e) are imparted a momentum of $|\hbar\vec{k}_r|=m_e\sqrt{2E_r/M}$ from a recoil of energy E_r. Usually, $\vec{k}_r\cdot\vec{x}$ is assumed to be sufficiently small so that $e^{-i\vec{k}_r\cdot\vec{x}}\approx 1$. However, expanding to first order in $\vec{k}_r\cdot\vec{x}$ gives

$$P_{if}(\vec{k}_r)\approx|\langle\psi_i|\psi_f'\rangle|^2+|\vec{k}_r|^2|\langle\psi_i|\hat{k}_r\cdot\vec{x}|\psi_f'\rangle|^2, \tag{8}$$

where $\hat{k}_r=\vec{k}_r/|\vec{k}_r|$. The first term is due to orbital mismatch and we use it to calculate the charge-state distribution. The second term is proportional to the recoil nucleus's energy (and is of order $|\vec{k}_r|^2a_0^2Z^{2/3}\sim 10^{-3}$ for^{21}Na) and is used to estimate the magnitude of recoil ionization.

A. Charge-state distribution

The charge-state distribution is calculated using a Monte Carlo technique and assuming a two-step ionization process consisting of electron shake-off due to orbital mismatch followed by Auger transitions. After determining the electron loss in 10^8 decays, the distribution is determined from the fraction of daughters in each charge state.

In the first step of the calculation, a Ne orbital is selected for each electron with probabilities determined from the orbital overlaps. Orbital occupancy is limited to 1. The single electron wave functions used for the ground states of Na and Ne were calculated using the Roothaan-Hartree-Fock expansion technique [55]. Principal quantum number $n=3$ orbitals have not been calculated for Ne, so we use $n=3$ orbitals for Mg to estimate the overlaps with ground-state Na orbitals. We assume electrons not retained in an $n\leqslant 3$ shell go to an autoionizing state or to the continuum. As we will find, the calculations agree with the experimental results only when the overlaps with $n=3$ Ne orbitals are also zero.

Additional ionization from rapid ($\lesssim 0.1$ ns [56]) Auger processes and associated shake-off is included as a second step. A number of calculations of these vacancy cascades have been performed [41,57,58] with results in reasonable agreement with experiment [59]. For each inner shell vacancy, additional electron loss is included according to the probabilities calculated in Ref. [58] or measured in Ref. [59].

The charge-state distribution is summarized in Table III. The calculation agrees with data only if all electrons in n

TABLE III. Charge-state distribution branching ratios (%), with and without Auger ionization effects.

	Including $n=3$		Neglecting $n=3$			Experimental
Charge	Without Auger	With Auger [a]	Without Auger	With Auger [a]	With Auger [b]	results
-1[c]	70.18	70.18	0.0	0.0	0.0	0.0
0	22.31	22.31	78.32	78.32	78.32	78.0 ± 3.1
1	6.34	4.74	19.41	17.80	17.99	18.6 ± 2.6
2	1.10	2.02	2.13	3.06	2.98	3.11 ± 0.44
3	0.067	0.60	0.14	0.66	0.60	0.266 ± 0.037
4	0.0023	0.13	0.0056	0.14	0.098	0.024 ± 0.006
5	0.00006	0.022	0.00017	0.023	0.012	0.011 ± 0.006
6	$<10^{-5}$	0.0030	$<10^{-5}$	0.0033	0.0014	$\leqslant0.010$

[a]Auger ionization from Ref. [59].
[b]Auger ionization from Ref. [58].
[c]Indistinguishable from neutrals because of short lifetime.

$\geqslant 3$ shells are ejected, although in either case the production of states with charge $\geqslant 3$ is overestimated. This is not surprising, because the Auger ionization data used pertain to single orbital vacancies, and we expect electron loss to decrease with increasing ionization state.

B. Recoil ionization

The second term has the form

$$P_{if}^{\text{recoil}}(E_r)=|\vec{k}_r|^2|\langle\psi_i|\hat{k}_r\cdot\vec{x}|\psi_f'\rangle|^2 =\frac{2E_r m_e^2}{\hbar^2 M}\left|\sum_n \langle\psi_i|\psi_n'\rangle\langle\psi_n'|\hat{k}_r\cdot\vec{x}|\psi_f'\rangle\right|^2. \quad (9)$$

Making the approximation $\langle\psi_i|\psi_n'\rangle\approx\delta_{in}$, we find

$$P_{if}^{\text{recoil}}(E_r)\approx\frac{3m_e}{M}\left(\int_{I_P}^{\infty}\frac{df_{\text{osc}}}{dE_{if}}E_{if}^{-1}dE_{if}\right)E_r, \quad (10)$$

where df_{osc}/dE_{if} is the differential oscillator strength, E_{if} the energy difference between initial and final states, and I_P the ionization potential. This perturbation increases with decreasing binding energy. The percentage increase I_q in the production of charge-state q for the highest-energy recoils compared to zero energy recoils is

$$I_q=100\times P_{if}^{\text{recoil}}(E_r^{\max})\frac{(\Gamma_{q-1}-\Gamma_q)}{\Gamma_q}, \quad (11)$$

where Γ_q is the branching ratio to ions of charge q and $E_r^{\max}$ is the maximum recoil energy.

The calculation is tested against the measured recoil ionization for ^{6}He. Using measured oscillator strengths for Li^+ transitions [60], we calculate $I_{1+}\approx 0.38\%$. This crude calculation achieves 60% of the experimentally determined value of $0.63\pm0.10\,\%$ [3]. The large nuclear velocities resulting from a decay with a large E_0 and small M enhance the effect.

For ^{21}Na we obtain $I_{1+}\approx 0.6\%$, using measured oscillator strengths for neutral Ne transitions to the continuum [61] and the measured charge-state branching ratios. In general, this effect is ≈ 4 times larger for singly charged ions from β^+ decay compared to β^- decay of identical E_0 and M, because of the smaller branching ratios to positive ions and lower daughter binding energies. Although inconsequential to the charge-state distribution, it is a potentially large systematic effect for β decay correlation experiments currently attaining the 0.01 level and seeking to reach precision of 0.001. An I_{1+} of 1% would lead to a systematic error of ≈ 0.005 in the β-ν correlation coefficient. The results of this calculation for the β^+ unstable nuclei ^{21}Na, ^{38m}K [10], ^{37}K [10], ^{82}Rb [62] and ^{78}Rb [10] (using experimentally determined Ar and Kr oscillator strengths [63]), each of which are currently being trapped for precision β decay studies, are shown in Table IV. For one- and two-electron systems, precise calculations of recoil induced ionization have been performed [23] but no such calculations exist for systems with $\geqslant 3$ electrons. More detailed calculations or precise measurements of recoil ionization will be necessary to interpret the results of future β decay correlation experiments.

TABLE IV. Percentage increase in production of $+1$ ions between highest- and lowest-energy recoils, I_{1+}, for various β^+ emitters currently being trapped.

Isotope	$E_r^{\max}$ (eV)	I_{1+} (%)
^{21}Na	229	0.6
^{38m}K	429	3.1
^{37}K	458	3.4
^{82}Rb	98	1.3
^{78}Rb	103	1.5

VI. CONCLUSION

Measurement of the charge-state distribution in ^{21}Na shows that $\approx 20\%$ of the decays shake-off $\geqslant 2$ electrons,

leading to positive ions, compared with only $\approx 5\%$ of β^- decays in which two or more electrons are lost. This is fortuitous for experiments that detect positive daughter ions. At the current level of precision obtained by these experiments (0.01 for the β-ν correlation), the independence of the charge-state distribution of the energies of the β and recoil ion is sufficient. However, a rough calculation indicates that the influence of the nuclear recoil on the ionization process cannot be ignored for measurements of β correlations using β^+ emitters surpassing the level of 0.01 and needs to be studied further. For β^- emitters, however, the effect is smaller since all decays result in positive ions. For β^+ decays that yield stable negative ions, such as ^{19}Ne [64], the impact of recoil ionization is uncertain, because of the competing effects of a large branching ratio to negative ions and small orbital binding energies. The β energy dependence of ionization is small ($\lesssim 1\%$) as expected in ^{21}Na but could be significant for decays with low Q values or high Z.

ACKNOWLEDGMENTS

We thank Jason T. Burke for his help with the ion source during the MCP calibration. We appreciate the assistance of the technical staff at the 88-in. cyclotron. This work was supported by the Director, Office of Science, Office of Basic Energy Sciences, U.S. Department of Energy under Contract No. DE-AC03-76SF00098.

[1] J.S. Allen *et al.*, Phys. Rev. **116**, 134 (1959).
[2] B.W. Ridley, Nucl. Phys. **25**, 483 (1961).
[3] C.H. Johnson, F. Pleasonton, and T.A. Carlson, Phys. Rev. **132**, 1149 (1963).
[4] T.A. Carlson, Phys. Rev. **132**, 2239 (1963).
[5] W.P. Alford and D.R. Hamilton, Phys. Rev. **105**, 673 (1957).
[6] M.M. Hindi *et al.*, Phys. Rev. C **58**, 2512 (1998).
[7] M. Trinczek *et al.*, Phys. Rev. Lett. **90**, 012501 (2003).
[8] P. Delahaye *et al.*, Hyperfine Interact. **132**, 479 (2001).
[9] D. Beck *et al.*, Nucl. Phys. A **701**, 369 (2002).
[10] A. Gorelov *et al.*, Hyperfine Interact. **127**, 373 (2000).
[11] T.A. Carlson, F. Pleasonton, and C.H. Johnson, Phys. Rev. **129**, 2220 (1963).
[12] T.A. Carlson, Phys. Rev. **130**, 2361 (1963).
[13] A.H. Snell and F. Pleasonton, Phys. Rev. **107**, 740 (1957).
[14] T.A. Carlson, Phys. Rev. **131**, 676 (1963).
[15] O. Kofoed-Hansen, Phys. Rev. **96**, 1045 (1954).
[16] A.H. Snell and F. Pleasonton, Phys. Rev. **100**, 1396 (1955).
[17] F. Pleasonton and A.H. Snell, Proc. R. Soc. London, Ser. A **241**, 141 (1957).
[18] A.H. Snell and F. Pleasonton, Phys. Rev. **111**, 1338 (1958).
[19] A.H. Snell, F. Pleasonton, and J.L. Need, Phys. Rev. **116**, 1548 (1959).
[20] P.M. Endt, Nucl. Phys. A **521**, 1 (1990).
[21] P. Stephas and B. Crasemann, Phys. Rev. **164**, 1509 (1967).
[22] Y. Isozumi, T. Mukoyama, and S. Shimizu, Phys. Rev. Lett. **29**, 298 (1972).
[23] L. Wauters *et al.*, J. Phys. B **30**, 4569 (1997).
[24] T. Mukoyama and S. Ito, Phys. Lett. A **131**, 182 (1988).
[25] Z.-T. Lu *et al.*, Phys. Rev. Lett. **72**, 3791 (1994).
[26] M. Rowe *et al.*, Phys. Rev. A **59**, 1869 (1999).
[27] H.C. Straub *et al.*, Rev. Sci. Instrum. **70**, 4238 (1999).
[28] S. Yagi *et al.*, Nucl. Instrum. Methods Phys. Res. B **183**, 476 (2001).
[29] R.S. Gao *et al.*, Rev. Sci. Instrum. **55**, 1756 (1984).
[30] T. Sakurai and T. Hashizume, Rev. Sci. Instrum. **57**, 236 (1986).
[31] A. Muller, N. Djuric, G.H. Dunn, and D.S. Belic, Rev. Sci. Instrum. **57**, 349 (1986).
[32] A. Bader *et al.*, Meas. Sci. Technol. **6**, 959 (1995).
[33] B. Brehm, J. Grosser, T. Ruscheinski, and M. Zimmer, Meas. Sci. Technol. **6**, 953 (1995).
[34] J. Oberheide, P. Wilhelms, and M. Zimmer, Meas. Sci. Technol. **8**, 351 (1997).
[35] I. Kawrakow, Med. Phys. **27**, 485 (2000).
[36] H. Behrens and J. Jänecke, *Numerical Tables for Beta-Decay and Electron Capture* (Springer-Verlag, New York, 1969).
[37] B.R. Holstein, Rev. Mod. Phys. **46**, 789 (1974).
[38] F. Glück, Comput. Phys. Commun. **101**, 223 (1997).
[39] T. Luhmann, Rev. Sci. Instrum. **68**, 2347 (1997).
[40] I.M. Band, M.B. Trzhaskovskaya, and M.A. Listengarten, At. Data Nucl. Data Tables **18**, 433 (1976).
[41] A.G. Kochur, V.L. Sukorukov, A.I. Dudenko, and P.V. Demekhin, J. Phys. B **28**, 387 (1995).
[42] C.F. Bunge, M. Galan, R. Jauregui, and A.V. Bunge, Nucl. Instrum. Methods Phys. Res. **202**, 299 (1982).
[43] Y.K. Bae, J.R. Peterson, A.S. Schlachter, and J.W. Stearns, Phys. Rev. Lett. **54**, 789 (1985).
[44] T.M. Stephen and B.L. Peko, Rev. Sci. Instrum. **71**, 1355 (2000).
[45] J.S. Levinger, Phys. Rev. **90**, 11 (1953).
[46] E.L. Feinberg, J. Phys. (Moscow) **4**, 423 (1941).
[47] R.L. Intemann, Phys. Rev. A **28**, 1288 (1983).
[48] I.S. Batkin, K.A. Bushahma, T.A. Churakova, and S.L. Demakov, J. Phys. G **18**, 1995 (1992).
[49] S.K. Nha, G. Schupp, and H.J. Nagy, Phys. Rev. C **27**, 1276 (1985).
[50] R.D. Scott, J. Phys. G **9**, 303 (1983).
[51] R.D. Scott, J. Phys. G **6**, 1427 (1980).
[52] G. Schupp and M.S Freedman, Phys. Rev. C **21**, 348 (1980).
[53] E.L. Feinberg, Sov. J. Nucl. Phys. **1**, 438 (1965).
[54] L. Giudicotti, M. Bassan, R. Pasqualotto, and A. Sardella, Rev. Sci. Instrum. **65**, 247 (1994).
[55] E. Clementi and C. Roetti, At. Data Nucl. Data Tables **14**, 177 (1974).
[56] K.R. Karim and L. Logan, Phys. Scr. **58**, 574 (1998).
[57] G. Omar and Y. Hahn, Z. Phys. D: At., Mol. Clusters **25**, 31 (1992).
[58] A. El-Shemi, Y. Lofty, and G. Zschornack, J. Phys. B **30**, 237 (1997).

[59] T.A. Carlson, W.E. Hunt, and M.O. Krause, Phys. Rev. **151**, 41 (1966).
[60] E. Hollauer and M.A.C. Nascimento, Phys. Rev. A **42**, 6608 (1990).
[61] W.F. Chan, G. Cooper, X. Guo, and C.E. Brion, Phys. Rev. A **45**, 1420 (1992).
[62] S.G. Crane *et al.*, Phys. Rev. Lett. **86**, 2967 (2001).
[63] W.F. Chan *et al.*, Phys. Rev. A **46**, 149 (1992).
[64] D.R. Maxson, J.S. Allen, and W.K. Jentschke, Phys. Rev. **97**, 109 (1955).